New Insights into Lamellar Structure Development and SAXS/WAXD Sequence Appearance during Uniaxial Stretching of Amorphous Poly(ethylene terephthalate) above Glass Transition Temperature

Daisuke Kawakami,[†] Christian Burger,[‡] Shaofeng Ran,[‡] Carlos Avila-Orta,[‡] Igors Sics,[‡] Benjamin Chu,[‡] Shu-Min Chiao,[§] Benjamin S. Hsiao,*[,‡] and Takeshi Kikutani*[,∥]

Research and Management Division, Toray Industries, Inc., 1-1-1 Sonoyama, Otsu, Shiga 520-8558, Japan, Department of Chemistry, Stony Brook University, Stony Brook, New York 11794-3400, Department of Chemical Engineering, Tunghai University, Taichung, Taiwan, and Department of Organic and Polymeric Materials, Tokyo Institute of Technology, O-okayama, Meguro-ku, Tokyo 152, Japan

Received November 18, 2007; Revised Manuscript Received January 22, 2008

ABSTRACT: An in situ study of structure formation in amorphous poly(ethylene terephthalate) (PET) during uniaxial stretching at a temperature 30 °C above glass transition temperature was carried out using synchrotron small-angle X-ray scattering (SAXS) and wide-angle X-ray diffraction (WAXD) techniques. Three major deformation-induced structure transitions were confirmed. (1) At small strains, the applied load increased initially but leveled off afterward. Sporadic isotropic crystallization without preferred orientation was observed by WAXD, where no hierarchical structure was seen by SAXS. (2) At intermediate strains, strain hardening took place. Although WAXD showed persistent progression of isotropic crystallization, SAXS indicated formation of a layered structure as well as a fibrillar domain in large scale. This behavior is not consistent with the mechanisms for shish-kebab or spinodal-assisted structure formation. Instead, it can be explained by flow-induced demixing of crystal and amorphous phases through layerlike flocking motion perpendicular to the stretching direction. (3) At high strains, the ratio between the applied load and strain was about constant. In this stage, crystal reorientation and lateral crystal growth took place. The corresponding structure changes could be categorized into three subregions. In the first region, the (010) crystalline plane began to orient. In the second region, the (100) crystalline plane began to orient. In the last region, the structure change became stable and the sample eventually broke apart.

Introduction

Poly(ethylene terephthalate) (PET) is a widely used engineering polymer with excellent mechanical properties and low cost. Its applications include fibers, films, and bottles. During the fabrication of these products, elongational deformation is used to enhance the mechanical properties, which can be directly related to the development of structure and orientation. The subject of stretching-induced crystallization in PET is thus of particular interest to both industry and academia.

Extensive studies of structure formation of PET during deformation have been carried out in the past.[1–9] Recently, the high intensity of synchrotron X-rays has been shown to be very effective to follow the real time development of structure and molecular orientation in polymers during processing.[10] Several in situ deformation studies of PET using synchrotron small-angle X-ray scattering (SAXS) and wide-angle X-ray diffraction (WAXD) techniques were carried out.[11–14] These studies indicated that uniaxial stretching (tensile deformation) first induces a mesophase structure, which is the precursor to crystallization. Since many industrial processes in PET compounding start from the amorphous solid state, in situ studies were also conducted to simulate the solid state deformation conditions.[15–26] For example, Blundell et al. used synchrotron WAXD measurement to investigate the structure development during fast drawing of amorphous PET films at varying temperatures around the glass transition temperature (T_g).[15–21] They reported that the deformation induced a smectic structure, which was then transformed into the triclinic crystalline structure. Chaari et al. reported the in situ WAXD study of PET during uniaxial deformation above T_g.[22] Although similar experimental observations were made, no detailed molecular information was extracted from the WAXD data.

In our laboratory, we also investigated the structure changes in amorphous PET samples during uniaxial stretching at temperatures below and above T_g (i.e., at 70, 90, and 100 °C, where T_g is about 80 °C) using combined WAXD, SAXS, and Raman spectroscopy methods.[23–26] We summarized a dynamic "phase diagram" to describe the varying structure changes under deformation,[25] where structures include amorphous, nematic, smectic, and triclinic crystal phases. The observed structure characteristics could correspond well with the mechanical behavior. The load−strain curves were thus categorized into three zones, namely, the constant load zone (I), the strain-hardening zone (II), and the constant load−strain ratio zone (III). The molecular mechanism for the structure change within each zone was proposed. It is imperative to point out that, despite the similarities of the load−strain curves obtained under different temperatures, the corresponding structures and their transformation pathways are quite different.

During polymer processing, semicrystalline materials can be shaped at temperatures between T_g and T_c (crystallization temperature). If the temperature is below T_g, the internal stress of the material would be too high to maintain a continuous process. If the temperature is above T_c, polymer can crystallize too fast, which would disturb the high stretch ratio deformation. In our previous studies,[23,25,26] we reported the structure development of PET under relatively slow uniaxial deformation just above T_g. The purpose of the present study is to further

* To whom correspondence should be addressed. Phone: +1-631-632-7793 (B.S.H.); +81-3-5734-3659 (T.K.). Fax: +1-631-632-6518 (B.S.H.); +81-3-5734-3659 (T.K.). E-mail: bhsiao@notes.cc.sunysb.edu (B.S.H.); tkikutan@o.cc.titech.ac.jp (T.K.).
[†] Toray Industries, Inc.
[‡] Stony Brook University.
[§] Tunghai University.
[∥] Tokyo Institute of Technology.

10.1021/ma702554t CCC: $40.75
Published on Web 03/26/2008

understand the initial structure formation in amorphous PET at the rubbery state under conditions that crystallization is severely depressed. We again used a relatively slow deformation rate, which was essential to acquire high quality scattering and diffraction data for quantitative analysis. For this purpose, the crystallization was chosen to be 110 °C, i.e., about 30 °C above T_g. The SAXS/WAXD results were carefully analyzed to verify the previously proposed mechanisms.[23–27] In addition, we paid extra attention to compare our results to the mechanisms of shish-kebab formation[28,29] and of spinodal decomposition,[30,31] as the former is generally considered the driving force to form lamellar structure and the latter has been widely acknowledged as a likely pathway to form the precursor structure of PET.

Experimental Section

Sample Preparation. The chosen PET sample was specially prepared by Toray Industries Inc., Japan. The sample had a minimal amount of catalysts but no additives. The weight-averaged molecular weight of the sample was about 25 000 g/mol. The procedure for sample preparation has been described earlier.[23–26] In brief, the PET pellets were first dried in vacuum at 150 °C for 6 h and were allowed to crystallize in air subsequently at 120 °C for 3 h. The crystallized sample was then molded into a dog-bone shape at 270 °C, followed by rapid quenching with ice water. No residual crystallinity was detected in the molded specimens by WAXD. The effective length of the specimen in deformation was 25 mm long. The specimen thickness was about 1 mm.

Experimental Procedures. The procedures for the deformation experiment were also similar to those employed in our previous studies,[23–26] except that the temperature was set at 110 °C. A modified Instron 4410 machine that allowed symmetric elongation of the specimen for SAXS/WAXD measurements was used.[27] The focused X-ray beam always illuminated on the same position of the specimen during deformation. The environmental chamber of the deformation apparatus was controlled using dry hot nitrogen gas. In the typical experiment, the specimen was first equilibrated in the chamber for 3 min at the desired temperature prior to deformation. The deformation rate was 20%/min, allowing the elongation time to last about 30 min before the sample breakage. To confirm the crystallization behavior of isotropic sample, a specimen annealed at 110 °C for 40 min without deformation was also examined by SAXS/WAXD measurements. Results indicated that the chosen thermal treatment could not produce any observable structure changes without deformation. However, due to the very slow deformation applied, it is not easy to separate the contributions from deformation and thermal annealing to crystallization. As we recognized the difficulty, an additional experiment investigating the structure formation during relaxation was also carried out.

In Situ Synchrotron X-Ray Measurements. Synchrotron X-ray measurements were carried out at the X27C beamline in the National Synchrotron Light Source (NSLS), Brookhaven National Laboratory (BNL). The wavelength of the X-ray was 1.366 Å. Two-dimensional WAXD and SAXS images were collected with an X-ray CCD detector (MarUSA) with resolution times of 20 and 60 s, respectively. The sample-to-detector distance for WAXD was 121 mm, while that for SAXS was 1814 mm. The diffraction angle in WAXD was calibrated using a polypropylene standard and an Al_2O_3 standard from National Institute of Standards and Technology. The scattering angle in SAXS was calibrated by a AgBe standard. The WAXD and SAXS measurements were carried out separately with different specimens under the same sample preparation and experimental conditions.

WAXD Data Analysis. We assume that the structure change in the deformed PET sample had a cylindrical (fiber) symmetry, which was confirmed by the similar X-ray images obtained from face-on and sectioned edge-on directions. The experimental 2D WAXD images (after the background and beam fluctuation corrections) were first separated into isotropic and anisotropic fractions, using an image analysis method described elsewhere.[27] The integrated intensity profiles for both fractions were subsequently estimated

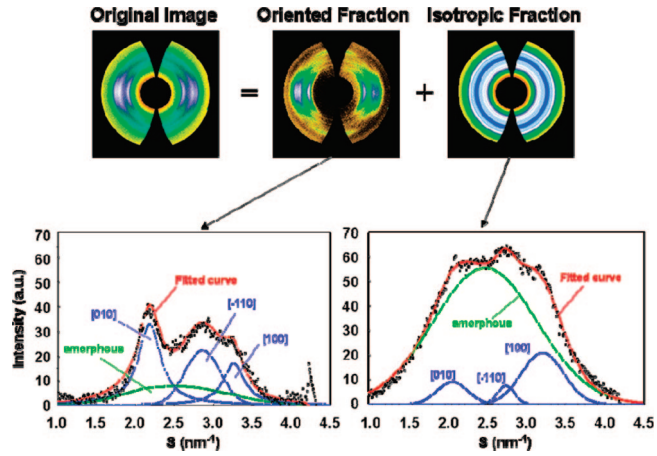

Figure 1. (a) 2D deconvolution of a typical WAXD image (measured at 410% strain) into oriented and isotropic fractions. (b) Peak fittings of integrated intensity profiles from the oriented fraction and the isotropic fraction. Both profiles were fitted with (010), (−110), and (100) crystalline peaks and one amorphous peak.

using the sin(ϕ) weight-average method[32,33] to correct the flat-plate detection geometry. This correction method can be considered as the simplified version of the Fraser correction, which has also been used by us before.[12] We found that the two methods yielded similar results, but the sin(ϕ) method expressed below is significantly easier.

$$I(s) = \int I(s,\phi)\,\sin(\phi)\,\mathrm{d}(\phi) / \int \mathrm{d}(\phi) \qquad (1)$$

where I represents the integrated intensity of the WAXD fraction, ϕ is the azimuthal angle with respect to the meridian ($\phi = 0$), and s ($=2\lambda^{-1}\sin\phi$, where λ is the wavelength of the X-ray and θ is half the scattering angle) is the scattering vector.

The integrated intensity profile for each fraction was deconvoluted into crystalline peaks and one oriented amorphous peak using a peak-fitting program (Grams 32 software, Galactic Industries Corporation). The procedure of this analysis is shown in Figure 1. The 2D WAXD image was first separated into two fractions: oriented fraction and isotropic fraction. The 1D integrated intensity profiles were then calculated using eq 1, and were deconvoluted into crystalline and amorphous peaks. In the deconvolution process, three crystalline peaks ((010), (−110), (100)) and one amorphous peak were used. Typically, crystalline peaks were much stronger than the amorphous peak in the oriented fraction, while the amorphous peak dominated in the isotropic fraction. We noticed that the positions of the crystalline peaks were consistent with those reported before for PET.[34] No (−103) peak was identifiable in the strain hardening zone, which was probably because the peak position of (−103) was very close to that of the (100) peak. Thus, the (100) intensity might be slightly overestimated in this study. All peaks in the integrated intensity profile were fitted by a mixed function of Gaussian and Lorenzian:

$$f_{\mathrm{MIX}} = (1 - M)\,(\mathrm{Gaussian}) + M\,(\mathrm{Lorenzian}) \qquad (2)$$

where M is the weight fraction of the Lorenzian function.[35–40]

The intensities of (010), (−110), and (100) peaks and the amorphous peak from the oriented fraction are symbolized as $I_{O(010)}$, $I_{O(-110)}$, $I_{O(100)}$, and I_{OA}, respectively. Similarly, the intensities of these peaks from the isotropic fraction are symbolized as $I_{I(010)}$, $I_{I(-110)}$, $I_{I(100)}$, and I_{IA}, respectively. The total crystallinity of the specimen was evaluated on the basis of the following expression:

$$\begin{aligned}\text{crystallinity} = [(I_{O(010)} + I_{O(-110)} + I_{O(100)}) + (I_{I(010)} + I_{I(-110)} + I_{I(100)})]/[(I_{O(010)} + I_{O(-110)} + I_{O(100)} + I_{OA}) + (I_{I(010)} + I_{I(-110)} + \\ I_{I(100)} + I_{IA})] \qquad (3)\end{aligned}$$

To facilitate the discussion on the distribution of oriented crystals, we further defined a term, "oriented crystalline ratio (OCR)", to

represent the ratio of each crystalline peak (in this case (010) and (100)) in the oriented fraction:

$$\mathrm{OCR}_{(010)} = I_{\mathrm{O}(010)}/(I_{\mathrm{O}(010)} + I_{\mathrm{I}(010)}) \quad (4)$$

$$\mathrm{OCR}_{(100)} = I_{\mathrm{O}(100)}/(I_{\mathrm{O}(100)} + I_{\mathrm{I}(100)}) \quad (5)$$

We chose and analyzed two crystalline peaks, 010 and 100, because of their importance of molecular interpretation. The direction of the vector normal to the 100 plane approximately coincides with that of benzene stacking, and the direction of the vector normal to the 010 plane approximately parallels the benzene ring.[23–25]

The crystal orientation in the oriented fraction was also calculated from the azimuthal scan $I(\phi)$ of two principle equatorial peaks, (100) and (010). The Grams 32 program was used for the curve fitting, which was based on the assumption that (100) and (010) peaks did not split near the equator. The crystal orientation could be expressed by the Hermans' orientation function (f_{Hermans})[32]

$$f = \frac{3\langle\cos^2\phi\rangle - 1}{2} \quad (6)$$

where

$$\langle\cos^2\phi\rangle$$

was defined as

$$\langle\cos^2\phi\rangle = \frac{\int_0^{\pi/2} I(\phi)\cos^2\phi\sin\phi\,\mathrm{d}\phi}{\int_0^{\pi/2} I(\phi)\sin\phi\,\mathrm{d}\phi} \quad (7)$$

The d-spacing of the crystallite was determined from the position of the fitted crystalline peak in the integrated profile using Bragg's law. The crystal sizes were estimated from the full width at half-height (fwhh) of the fitted crystalline peaks using the Scherrer equation. The Scherrer equation can be expressed as[32]

$$D_{hkl} = K\lambda/(\beta_{1/2}\cos\theta) \quad (8)$$

where D_{hkl} represents the apparent lateral crystallite size of the hkl reflection plane and $\beta_{1/2}$ is the fwhh of the diffraction peak hkl in radians. The shape factor K was set as 0.9 for polymer systems. We recognize that there might be lattice distortion due to the broadening of line width, which could lead to an underestimation of the crystal size. According to Salem,[41,42] however, the contribution of the lattice distortion was small.

SAXS Data Analysis. The contribution of air scattering was first removed by subtracting the air reference from the measured SAXS image.[12] The invariant (Q) was evaluated in the custom way ($Q = \int I(q)q^2\,\mathrm{d}q$, where $I(q)$ is the intensity of the scattered X-ray and $q = 2\pi s$). The long period (L) was estimated by the relationship $L = 2\pi/q_{\max}$, where $q_{\max}$ represents the peak position in the Lorentz corrected scattering plot (i.e., Iq^2 vs q). By magnifying the center part of the SAXS images, we were able to deconvolute the image into isotropic and anisotropic fractions in the same manner as we did with the WAXD image. Typical patterns of the oriented fraction always exhibited a two-bar feature superimposed with an equatorial streak; the latter represents the fibril structures that will be discussed further.

Results and Discussion

There are two important but justifiable assumptions made in our analysis. The first is that no necking formation during deformation of the samples takes place (this was confirmed experimentally). Consequently, the local strain at the position where X-ray illuminated should be equivalent to the applied strain. The second assumption is that the deformed structure has a cylindrical symmetry. Although one would expect that the structural development should be asymmetric in the dog-bone specimen during stretching, the experimental results indicated that the asymmetry was low. This was also verified in our previous studies.[12,23–26]

It should be noted that relaxation and crystallization occur simultaneously during the experiment. Schultz et al. showed that crystallization of POY (partially oriented yarn: spun at 3000 m/min) of PET started within a very short time, between 50 and 100 ms at 100 °C and between 15 and 20 ms at 110 °C.[6] In addition, they also demonstrated a remelting phenomenon in samples that have experienced positive shrinkage using the PET POY samples at a similar temperature.[7] Due to the slow deformation chosen in the present study, it is difficult to separate the contributions of deformation and thermal annealing to the behavior of crystallization. It is necessary to point out that Schultz et al. had used POY as the starting material, while isotropic samples were chosen as the starting material. The two materials have some essential differences, as POY should possess a greater amount of pre-existent (embryo) nuclei than the isotropic sample before uniaxial stretching.

Three Zones in Structure Evolution during Stretching. The load−strain curve and selected oriented WAXD images taken during uniaxial stretching of the amorphous PET sample are shown in Figure 2. As mentioned earlier, the correlations between the mechanical behavior and structural development can be divided into three zones.[23–26] These zones include the constant load zone (I), the strain-hardening zone (II), and the constant load−strain ratio zone (III). Some differences in zone division between this work and the previous study were seen, and they are summarized in Table 1. In short, both zone I and zone II are shorter and the corresponding applied load is lower at higher temperature (i.e., 110 °C). In zone III, the strain-at-break ratios are almost the same at different temperatures, but the ultimate load is much lower at higher temperature. In spite of the similar features in load−strain curves at varying temperatures, it is imperative to note that the structure characteristics in each zone were quite different when the temperature changed, which will be discussed next. Figure 2 illustrates WAXD images from the oriented fraction collected over a 20 s time frame (i.e., the average structure evolution at 6.7% strain), from which the structure changes in each zone can be summarized as follows.

Zone I. The Persistent Appearance of Isotropic Crystallites. Zone I is defined as the region before strain hardening, where a constant load is reached (i.e., at strain between 0 and 80% in this work). In the first half of this zone, load increased rapidly to about 4 N and remained constant afterward. In Figure 2, two representative oriented WAXD images were illustrated in this zone. The first image was collected during the load increase, and the second image was collected at the constant load. It was very interesting to notice that both measured WAXD patterns exhibited distinct triclinic diffraction rings without preferred orientation (the weak residual "oriented feature" in Figure 2 was due to the polarization of the X-ray beam). In other words, the deformation-induced crystallinity in zone I was isotropic, and the amount increased with strain (or with time).

The above observation was quite different from our earlier results.[26] When the same sample was stretched at 90 °C, a considerable amount of oriented mesophase was found at the end of this constant load zone. LeBourvellec et al. showed the existence of a critical amorphous orientation for the initiation of crystallization by drawing of amorphous PET film below 103 °C.[3] However, in this study, we were not able to extract any oriented fraction from the WAXD images. We believe that the high mobility of PET molecules at elevated temperatures is responsible for the different structure development. During deformation, the stretched and oriented molecular segments can take place in both nucleation and growth processes. However, when the relaxation rate of the molecules exceeds the deformation rate of the sample at high temperatures, only the nucleation process can prevail. As a result, the subsequently grown crystallites involving relaxed chain segments are not oriented.

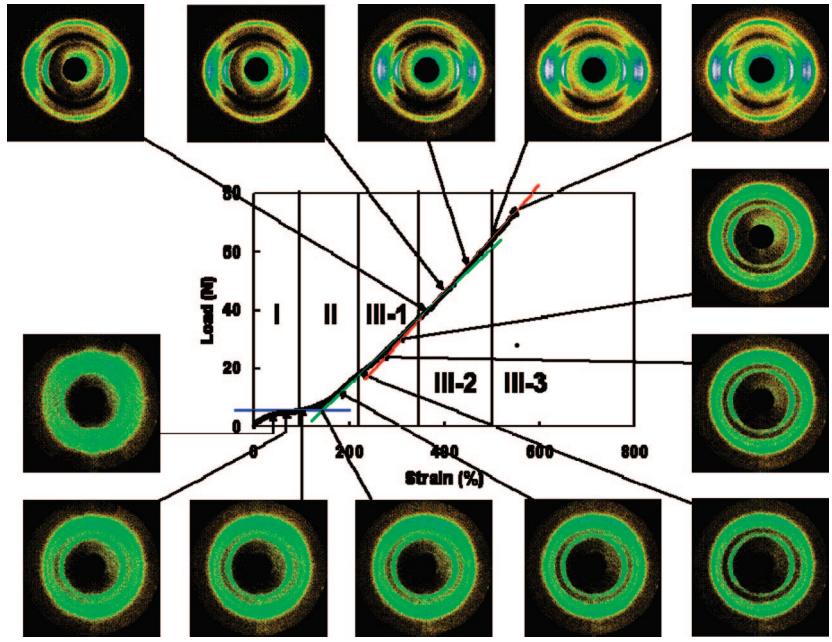

Figure 2. The load−strain curve and selected WAXD oriented images (after subtraction of the isotropic fraction). The arrows indicate the average position where each image was taken.

Table 1. Comparison of Categorization of Load−Strain Curves at Different Temperatures

test temperature (°C)	zone I		zone II		zone III	
	limiting strain (%)	limiting load (N)	limiting strain (%)	limiting load (N)	limiting strain (%)	limiting load (N)
90[a]	140	8	380	50	580	135
110[b]	80	4	220	18	580	78

[a] Data from ref 26. [b] Data from this work.

Figure 3 shows corresponding SAXS images taken under the same deformation conditions as in Figure 2 (SAXS and WAXD were not simultaneously measured). Since the collection time for SAXS was longer (60 s), each image represented the average behavior over a greater range of strain change. No discrete SAXS peak, typically observed from the lamellar morphology, could be found in these images. This suggested that the small isotropic crystallites (induced by deformation) were sporadically developed, whereby they were embedded in the amorphous matrix without forming higher order organization. Mechanically, these sporadic crystallites act as physical cross-linkers that would enhance the bulk strength. However, as the relaxation rate of the molecules is fast (the connectivity between the crystallites is thus weak), and the number as well as the size of these crystallites is probably small, such a "network" cannot bear much applied load.

Zone II. Formation of Anisotropic Layered Structure with Isotropic Crystallites. Zone II is the strain-hardening zone (strain between 80 and 220%). Both WAXD images in Figure 2 indicated that the crystalline structure in this zone remained to be isotropic. No preferred orientation for equatorial (100) or meridional (−103) peaks could be observed (again, the slightly higher intensity in the meridional direction was caused by the intrinsic polarization of synchrotron X-ray). The calculated crystallinity using eq 3 is shown in Figure 4. It was found that the crystallinity increased rapidly with strain, which exhibited a linear relationship. The increase in crystallinity apparently reinforced the "network" strength, resulting in the increase in load.

Some interesting features were found in the SAXS images (four representative SAXS images were shown) in Figure 3. The first SAXS image (at 90% strain) exhibited slight anisotropy with significantly enhanced scattered intensity. As deformation continued, stronger anisotropy in scattering feature was seen (the scattering shape changed from oval to dumbbell). The emergence of the meridional scattering peak resembled that of a layered structure. The linear intensity profiles on the meridian extracted from the SAXS images are illustrated in Figure 5. It was seen that, at strain below 110%, the intensity decreased monotonically with the scattering vector q. A scattering shoulder appeared at a strain of 130%, and it changed into a peak at higher strains with the peak position moving toward higher q. The position shift of the scattering peak suggested that the long period of the layered structure decreased with increasing strain. The changes of the long period with deformation strain are illustrated in Figure 6, showing a clear decrease in zone II.

Lee et al.[43,44] had carried out in situ light scattering (LS) and SAXS measurements of unoriented PET isothermally crystallized below T_c (including 110 °C). They reported the existence of "isolated domains" (40–60 nm diameters) containing initial crystallites. This scenario is also consistent with our observations; i.e., the growth of the sporadic isotropic crystallites in zone I eventually led to discrete domains in zone II. The application of uniaxial tensile deformation appears to flock the domains into a layered structure, oriented perpendicularly to the stretching direction. This process might be similar to the one observed by Hashimoto et al. in the study of shear-enhanced concentration fluctuations in semidilute polymer solution.[45] In Hashimoto's system, the anisotropic squeezing of the solvent played an important role to reorganize the concentrated domain, while, in our case, the flocking of crystallites (into a layered structure that aligned perpendicularly to the flow) may be due to the ease of stress relaxation in short range. We expect that, at higher strains, a higher degree of flocking took place, which is consistent with the observation that the long period decreased with increasing strain (Figure 6).

The SAXS invariant calculated at different strains is shown in Figure 7. It was seen that the invariant increased most dramatically in zone II compared with those in the other zones. The large invariant increase also agrees well with the flocking of crystalline domains into a layered structure, where the density contrast is significantly enhanced, resulting in the increase of the SAXS invariant.

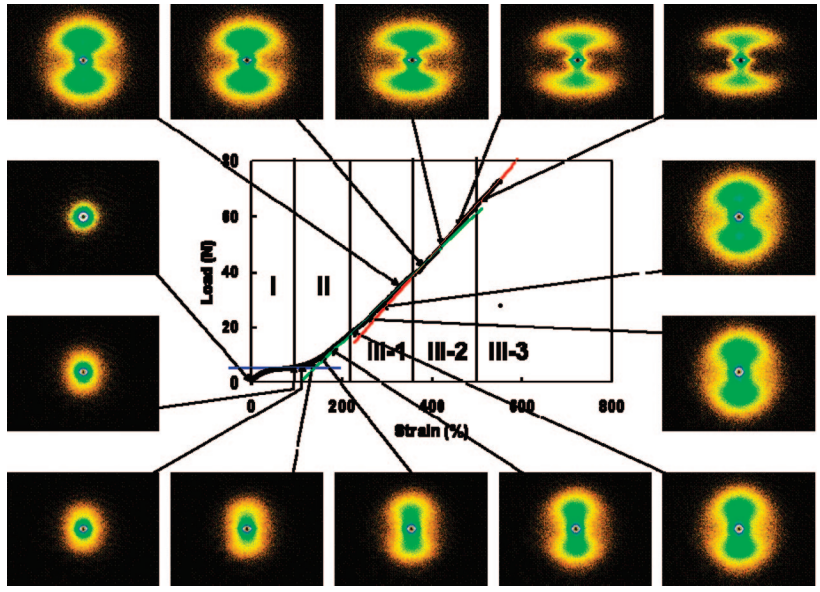

Figure 3. Selected SAXS images and the load−strain curve. The arrows indicate the average position where each image was taken.

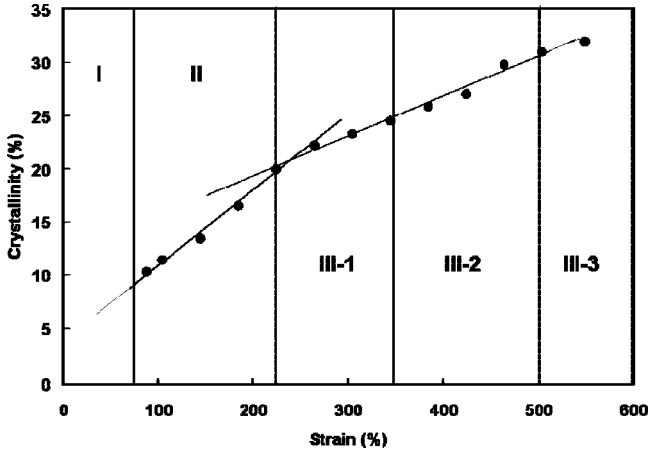

Figure 4. The change of crystallinity (from the WAXD analysis) as a function of applied strain.

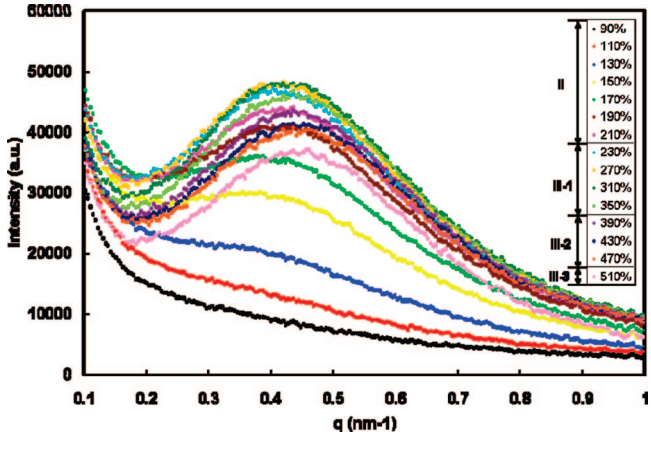

Figure 5. The intensity profiles along the meridional direction in SAXS at varying strains.

The observation that WAXD exhibited isotropic crystallinity while SAXS exhibited oriented layered structure cannot be explained by the conventional concepts of flow-induced shish-kebab formation or spinodal-assisted crystallization. This is because if the shish-kebab structure prevails, the corresponding WAXD results should exhibit oriented crystalline reflections,[28,29]

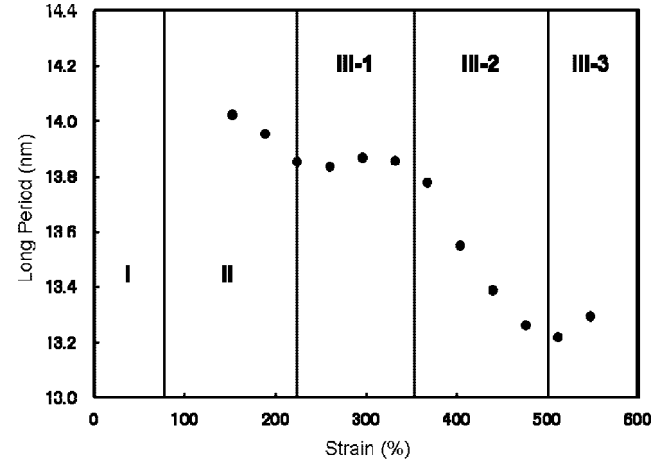

Figure 6. The change of long period as a function of applied strain.

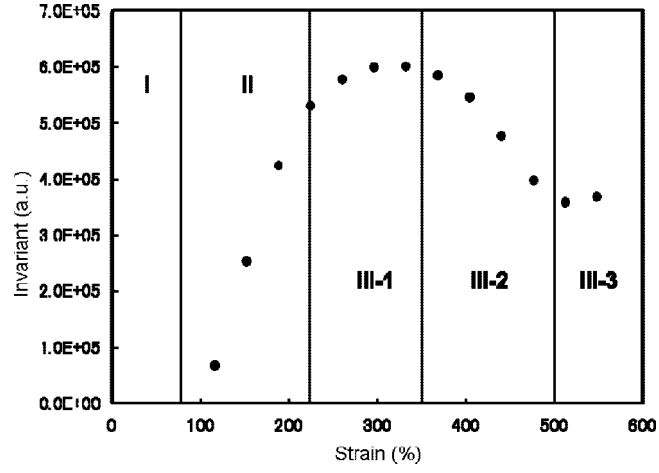

Figure 7. The change of the SAXS invariant as a function of applied strain.

but this was not seen. We can also rule out the structure formation through spinodal decomposition[30,31] because the layered SAXS pattern did not appear before the crystalline WAXD pattern.[46–49]

The SAXS images in Figure 3 consistently showed an equatorial streak. Two types of microstructures might be responsible for this feature: microvoids and fibrillar structure. Because no microvoids in the specimen could be observed by electron microscopy and the intensity of the streak was relatively weak, we feel the streak was most likely due to the fibrillar structure. Since the layered structure was in the scale of 10 nm and the fibril structure was in the scale of 100 nm, we propose the following hierarchical arrangement. The X-ray results can be best explained by the "para-crystalline stacking model" proposed by Bonart and Hosemann.[50] In this model, amorphous layers separate crystalline lamellae forming the stack structure, which is packed within the fibrillar microstructure. The fibrils are dispersed in the amorphous matrix with the long axis parallel to the stretching direction. Kubo et al. reported transformation of spherulites into rodlike morphology occurred in PET polymerized by Sb catalyst using opto-rheometry and Rayleigh scattering measurements at 110 °C.[51] We consider that the substantial transformation accompanying crystalline orientation starts at zone III in our study, and that the discovery of rodlike structure before crystalline reorientation is our new insight.

Zone III. Reorientation and Growth of Crystalline Domains. Zone III exhibits a constant load−strain ratio (at strains between 220 and 580%). In this zone, the SAXS patterns show a persistent layered structure, but the WAXD patterns exhibit a clear sign of crystallinity increase and orientation enhancement. On the basis of SAXS/WAXD results (especially the long period plot in Figure 6), zone III could be further categorized into three subregions: zone III-1, which exhibited a constant value of long period; zone III-2, which showed a decrease in long period with strain; and zone III-3, which showed the long period increase again. The corresponding characteristics of the development in crystal structures were very different in these subregions, which are summarized below.

1. Zone III-1. Increase of Oriented (010) Reflection. This subregion can be characterized by a stable layered structure (Figure 3) and a constant long period from the layered structure (Figure 6). However, distinct changes on the crystalline structure were noted by WAXD (Figure 2). It was seen that the intensity of the (010) reflection ring began to aggregate on the equator, which might have resulted from the combined effects of growth of oriented crystallites and reorientation of exiting crystallites. The crystallinity estimated from the sum of (010), (−110), and (100) is shown in Figure 4, which increased almost linearly with deformation but had a smaller slope than that in zone II. The difference in the rate of crystallization in zones II and III can be explained by the different crystallization schemes in these two zones. (1) In zone II, the small crystallites can aggregate through flocking, resulting in a layered structure oriented perpendicularly to the stretching direction. In this zone (as well as in zone I), deformation-induced nucleation is definitely the dominant process that is responsible for the faster crystallinity increase. (2) In contrast, the crystal reorientation and the lateral crystal growth are the dominant processes in zone III, which has a slower rate in crystallinity increase because the molecular chains need to rearrange and crystallize (even at 110 °C, the chain mobility is relatively low) in this study.

In Figure 2, a pair of distinct equatorial (010) reflections is seen. Quantitative results of OCR (oriented crystalline ratio), defined as the fractional ratio of the specific crystal reflection that remains in the anisotropic fraction, were obtained (Figure 8 shows the OCR values for crystal reflections (010) and (100) in zone III as functions of strain). It was seen that the value of OCR_{010} was near zero in zone II. In zone III, this value increased rapidly from 0.27 to ∼0.6 in zone III-1 and then leveled off around 0.81 in the middle of zone III-2. On the other hand, the value of OCR_{100} was smaller than OCR_{010} (it was barely visible in zones II and III-1, but it also increased in zone III-2 and

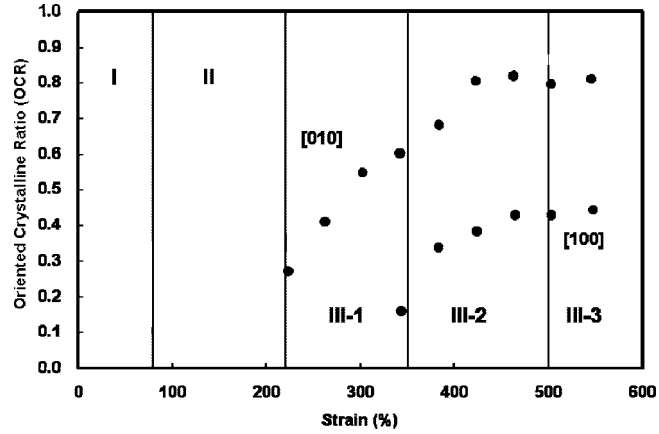

Figure 8. The changes of oriented crystalline ratio (OCR) for (100) and (010) reflections as a function of applied strain.

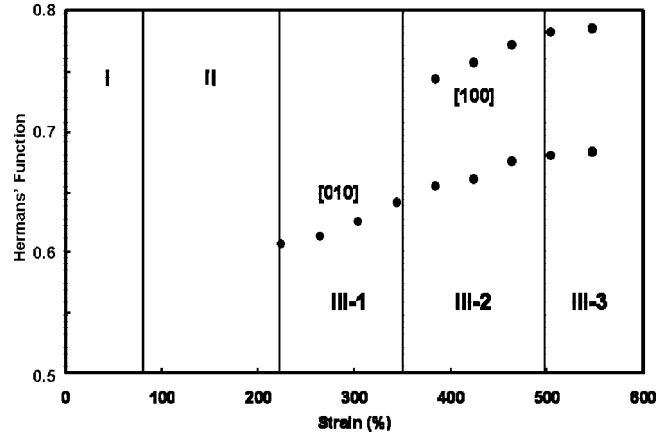

Figure 9. The changes of Hermans' function for (100) and (010) reflections as a function of applied strain.

leveled off at a lower value (∼0.43). This indicated that the (010) crystalline reflection was the characteristic feature in zone III-1.

The Hermans' function of the different crystal reflection was also calculated from 2D WAXD images, and results are illustrated in Figure 9. It is seen that both the $f_{Hermans}(010)$ and $f_{Hermans}(100)$ values increased with strain. $f_{Hermans}(010)$ started at ∼0.61 at the onset of zone III, increased almost linearly through zones III-1 and III-2, and finally leveled off in zone III-3 at ∼0.68. Since the crystalline reflection (100) was not observed in zone III-1, $f_{Hermans}(100)$ was determined only in zones III-2 and III-3. It was seen that $f_{Hermans}(100)$ increased from 0.74 to 0.78 and leveled off in zone III-3. In zone III, all crystallites were clearly oriented by deformation, but the crystals have their (100) reflection face oriented more than their (010) reflection face.

There are several possible pathways that can cause the (010) orientation: (1) reorientation of isotropic crystallites, (2) transformation from the isotropic amorphous phase to the oriented crystalline phase through the mesomorphic phase, and (3) direct crystallization from the isotropic amorphous phase to the oriented crystalline phase. Among these, pathway 1 is most consistent with the experimental observation; i.e., the WAXD intensity of the isotropic (010) fraction decreased from 8.1 to 4.6% (data not shown), and the corresponding Hermans' function showed an increase in orientation. We do not favor pathway 2 because no oriented mesomorphic signal was found from the WAXD analysis. Although pathway 3 cannot be ruled out, its contribution may be relatively small. This is because the value of OCR_{010} showed a rapid increase with strain, where

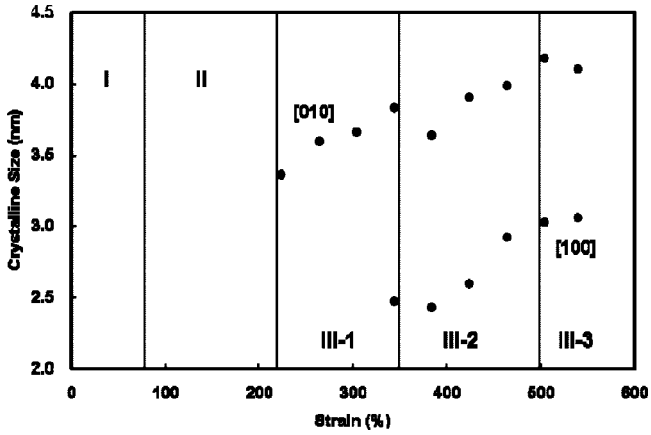

Figure 10. The changes of crystalline dimensions corresponding to the (100) and (010) reflections as a function of applied strain.

the degree of increase far exceeded the effect of direct crystallization. We thus argue that a significant fraction of the isotropic crystals became oriented under deformation but a small fraction of the isotropic amorphous phase also transformed into the oriented crystalline phase directly.

The observation that the anisotropy of the (010) reflection appeared earlier and at a higher degree than that of the (100) reflection could be explained as the following. It has been shown that the bonding force between the benzene ring stacking by induction interaction is weaker than that of benzene sheet structure caused by C═O dipole–dipole interactions.[23–26,52] The difference may be quite significant, especially in the initial stage of structural formation where distances among molecular chains are relatively large. As a result, stronger dipole–dipole interactions lead to earlier enhancement of the (010) anisotropy. In fact, the (010) reflection not only appeared earlier but the corresponding crystal dimension also become larger. Figure 10 shows the variation of oriented crystallite dimension (estimated by eq 8) for different crystal reflection as a function of deformation stain. The crystal dimension related to the (010) reflection was generally larger than 3.5 nm in zone III-1, but the dimension related to the (100) reflection was below 2.5 nm.

2. Zone III-2. Increase of Oriented (100) Reflection. Distinct features of fiber diffraction patterns were seen in zone III-2 (Figure 2), where the features could be mainly attributed to orientation of the (100) reflection on the equator. In this zone, the corresponding OCR_{100} value increased from 0.14 to 0.42 (Figure 8), $f_{Hermans}(100)$ increased from 0.72 to 0.78 (Figure 9), and the crystal dimension also increased more than 3 nm (Figure 10). Pathway 1 still appears to be a viable route, since the isotropic 100 intensity fraction dropped slightly from 6.2 to 5.1% in zone III-2. However, pathway 2 is also evident, since the oriented amorphous (or mesomorphic) fraction was clearly detected (see the left figure of Figure 1 showing 410% strain: zone III-2). The oriented mesomorphic phase would facilitate the formation of oriented crystallites, thus resulting in a high value of $f_{Hermans}(100)$ (Figure 9). The relatively low values of OCR_{100} (Figure 8) can be explained by the weak interactions between benzene rings in the unit cell structures. It is conceivable that the oriented amorphous fraction was necessary (as the precursor phase) to form ordered (100) stacks, which would render pathway 3 relatively unimportant.

Although we try to distinguish the strain-induced crystallization process with three different pathways, they are coupled closely together. When the isotropic crystals reorient (the dominant pathway in zone III-1), the process would generate oriented amorphous chains leading to further crystallization (the dominant pathway in zone III-2). This is consistent with the long period plot in Figure 6, where the long period was about constant in zone III-1 but continued to decrease in zone III-2. The decrease in long period is a sure sign of crystallinity increase in PET (also observed in Figure 4). The SAXS invariant (Figure 7) showed a slight increase in zone III-1 and a decrease in zone III-2, resulting in a maximum value. This can be explained by the argument that the production of the oriented amorphous (mesomorphic) phase in zone III-2 reduced the scattering contrast.

3. Zone III-3. Stabilization of Oriented Crystalline Structure. In the final stage of zone III-3, before the sample broke, both OCR (Figure 8) and the direction of the vector normal to Hermans' orientation function (Figure 9) from WAXD reached plateau values at a strain of about 500%, whereas the long period (Figure 6) and the invariant (in Figure 7) from SAXS began to rise after passing through respective minima. Similar phenomena were also observed in our previous studies at 70 and 90 °C.[26,27] These features appear to be universal in the final stage of deformation in semicrystalline PET prior to the tensile break. This behavior can be explained by the following. In zone III-3, the sample is dominated by the fibril structure. Most of the noncrystalline chains surrounding the crystallites are extended (forming the oriented amorphous phase) and there is not much room for the crystallites to further orient (OCR and Hermans' function thus reach plateau values). More extension of amorphous chains can increase the long period as well as the invariant (since the density contrast may also be enhanced) but eventually leads to catastrophic failure.

It is interesting to note that, at the final stage of deformation, the sample still possessed a large fraction of the isotropic amorphous phase (as evidenced by an isotropic halo in Figure 2), where the maximum crystallinity was only 32% (Figure 7) and the corresponding OCRs were below unity. We hypothesize that crystallization mainly occurs within the fibrillar superstructure in the final stage, where chain entanglements and tie chains all reach their limits for mechanical stability before chain breakage or crystalline structure disintegration. A large fraction of isotropic amorphous chains remain intact at the elevated temperature and they do not contribute to the load bearing.

Mechanism Responsible for the Strain-Induced Structure Change. The strain-induced structure changes in amorphous PET above its glass temperature can be summarized using a molecular model illustrated in Figure 11. The mechanical behavior is closely related to the structure changes.

Zone I: A small amount of isotropic crystallites begin to appear sporadically in the isotropic amorphous domain, where the stress may play a role to facilitate the nucleation process. No superstructure with 10 nm length scale such as lamellae or fibrils can be identified. The size and amount of the crystallites are so small such that they cannot function well as physical cross-linkers. The mechanical load is thus mainly supported by the molecular motion. Since the stress does not concentrate on the small crystallites, their orientation does not develop, and the applied load does not affect the structure formation.

Zone II: Spherical domains containing isotropic crystallites are formed initially, and then, the anisotropic fibril domains oriented along the extensional axis also appear. These fibrillar domains are embedded in the matrix of the isotropic amorphous phase. Within the fibrillar domain, isotropic crystallites formed a layered structure through the flocking motion during tensile elongation. Sample is significantly toughened by both fibrillar morphology and increased crystallinity marking the region of strain hardening.

Zone III: All crystallites began to orient. The oriented (010) reflection appears first in the beginning of this zone (zone III-1) and continues to increase through zone III-2. The oriented (100) reflection, on the other hand, appears only in zone III-2. More crystallites are developed within the fibrillar

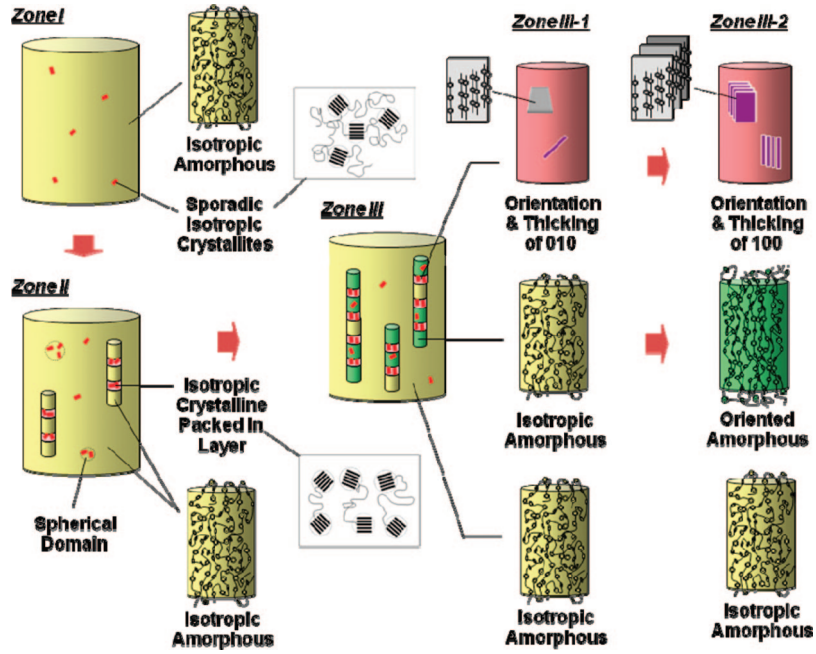

Figure 11. The proposed molecular structural models for zone I, II, III-1, and III-2.

domain, resulting in the decrease in long period. Finally, in zone III-3, the strain-induced crystalline structure and morphology appear to stabilize and the sample breaks apart eventually. In zone III, the applied load increases almost linearly with the applied strain. The mechanical hardening can be explained by both the crystallinity increase and the fibrillar formation induced by strain. However, a considerable amount of polymer chains remain to be the isotropic amorphous phase until they break.

Conclusions

An in situ study of structural formation of an amorphous poly(ethylene terephthalate) (PET) sample during uniaxial deformation at 110 °C was carried out using both wide-angle X-ray diffraction (WAXD) and small-angle X-ray scattering (SAXS) with synchrotron radiations. At this temperature, all structures developed were mainly induced by strain. The load−strain curve could be categorized into three zones based on the mechanical behavior and structure characteristics. Zone I is represented by sporadic isotropic crystallization in the isotropic amorphous phase. Except at the initial stage, the load was almost constant due to the absence of sufficient crystallites that can work as physical cross-linkers. In zone II, fibrillar domains containing isotropic crystallites are formed. The isotropic crystallites are arranged into a layered structure (perpendicular to the stretching direction) that is probably due to the flocking motion induced by stress. WAXD showed persistent progression of isotropic crystallization, but SAXS indicated a clear formation of layered structure and fibrillar domain. This behavior is not consistent with the mechanisms for shish-kebab or spinodal-assisted structure formation. As a result of crystal and fibril formations, which generate an effective physical network, load begins to increase significantly. Zone III is marked by a constant load−strain ratio, and can be further categorized into three regions. In the first region, the (010) reflection starts to orient, while the long period remains about constant. This region is dominated by the crystal reorientation process. In the second region, the (100) reflection also orients and the meridional long period decreases with strain. This region is dominated by the stress-induced crystallization probably through the precursor of the oriented amorphous or mesomorphic phase. In the final stage of zone III, all structure changes slow down and the sample breakage occurs eventually.

Acknowledgment. The authors thank the National Science Foundation (DMR-0405432) and the National Textile Center and the Toray Industry in Japan for financial support. The authors also thank Mr. Uchida from Toray for the synthesis of experimental PET samples and Dr. Dufei Fang for the assistance of the image analysis.

References and Notes

(1) Lapersonne, P.; Tassin, J. F.; Monnerie, L.; Beautemps, J. *Polymer* **1991**, *32*, 3331.
(2) Lapersonne, P.; Tassin, J. F.; Monnerie, L. *Polymer* **1994**, *35*, 2192.
(3) LeBourvellec, G.; Monnerie, L.; Jarry, J. P. *Polymer* **1986**, *27*, 856.
(4) Ward, I. M. *Polym. Eng. Sci.* **1984**, *24*, 724.
(5) Ajji, A.; Cole, K. C.; Dumoulin, M. M.; Ward, I. M. *Polym. Eng. Sci.* **1997**, *37*, 1801.
(6) Lee, K. G.; Schultz, J. M. *Polymer* **1993**, *34*, 4455.
(7) Peszkin, P. N.; Schultz, J. M. *J. Appl. Polym. Sci.* **1986**, *24*, 2591.
(8) Hristov, H. A.; Schultz, J. M. J. *Polym. Sci., Polym. Phys. Ed.* **1990**, *28*, 1647.
(9) Hristov, H. A.; Heatle, J. W. S.; Schultz, J. M.; Kennedy, A. D. *J. Polym. Sci., Part B: Polym. Phys.* **1995**, *33*, 125.
(10) Chu, B.; Hsiao, B. S. *Chem. Rev.* **2001**, *101* (6), 1727.
(11) Asano, T.; Balta-Calleja, F. J.; Flores, A.; Tanigaki, M.; Mina, M. F.; Sawatari, C.; Itagaki, H.; Takahashi, H.; Hatta, I. *Polymer* **1999**, *40*, 6475.
(12) Ran, S.; Wang, Z.; Burger, C.; Chu, B.; Hsiao, B. S. *Macromolecules* **2002**, *35*, 10102.
(13) Keum, J. K.; Kim, J.; Lee, S. M.; Song, H. H.; Son, Y.-K.; Choi, J.-I.; Im, S. S. *Macromolecules* **2003**, *36*, 9873.
(14) Fukao, K.; Koyama, A.; Tahara, D.; Kozono, Y.; Miyamoto, Y.; Tsurutani, N. *J. Macromol. Sci., Phys.* **2003**, *B42*, 717.
(15) Welsh, G. E.; Blundell, D. J.; Windle, A. H. *Macromolecules* **1998**, *31*, 7562.
(16) Welsh, G. E.; Blundell, D. J.; Windle, A. H. *J. Mater. Sci.* **2000**, *35*, 5225.
(17) Blundell, D. J.; Mahendrasingam, A.; Martin, C.; Fuller, W. *J. Mater. Sci.* **2000**, *35*, 5057.
(18) Mahendrasingam, A.; Blundell, D. J.; Martin, C.; Fuller, W.; MacKerron, D. H.; Harvie, J. L.; Oldman, R. J.; Riekel, C. *Polymer* **2000**, *41*, 7803.
(19) Blundell, D. J.; Mahendrasingam, A.; Martin, C.; Fuller, W.; MacKerron, D. H.; Harvie, J. L.; Oldman, R. J.; Riekel, C. *Polymer* **2000**, *41*, 7793 .

(20) Mahendrasingam, A.; Martin, C.; Fuller, W.; Blundell, D. J.; Oldman, R. J.; MacKerron, D. H.; Harvie, J. L.; Riekel, C. *Polymer* **2000**, *41*, 1217.
(21) Blundell, D. J.; MacKerron, D. H.; Fuller, W.; Mahendrasingam, A.; Martin, C.; Oldman, R. J.; Rule, R. J.; Riekel, C. *Polymer* **1996**, *37*, 3303.
(22) Chaari, F.; Chaouche, M.; Douset, J. *Polymer* **2003**, *44*, 473.
(23) Kawakami, D.; Ran, S.; Burger, C.; Fu, B.; Sics, I.; Hsiao, B. S. *Macromolecules* **2003**, *36*, 9275 .
(24) Kawakami, D.; Hsiao, B. S.; Ran, S.; Burger, C.; Fu, B.; Sics, I.; Chu, B.; Kikutani, T. *Polymer* **2004**, *45*, 905.
(25) Kawakami, D.; Hsiao, B. S.; Burger, C.; Ran, S.; Avila-Orta, C.; Sics, I.; Kikutani, T.; Jacob, K. I.; Chu, B. *Macromolecules* **2005**, *38*, 91.
(26) Kawakami, D.; Ran, S.; Burger, C.; Avila-Orta, C.; Sics, I.; Hsiao, B. S.; Chu, B.; Kikutani, T. *Macromolecules* **2006**, *39*, 2909.
(27) Ran, S.; Zong, X.; Fang, D.; Hsiao, B. S.; Chu, B.; Phillips, R. *Macromolecules* **2001**, *34*, 2569.
(28) Somani, R. H.; Yang, L.; Zhu, L.; Hsiao, B. S. *Polymer* **2005**, *46*, 8587.
(29) Hsiao, B. S.; Yang, L.; Somani, R. H.; Avila-Orta, C. A.; Zhu, L. *Phys. Rev. Lett.* **2005**, *94* (11), 000. 117802.
(30) Imai, M.; Mori, K.; Mizukami, T.; Kaji, K.; Kanaya, T. *Polymer* **1992**, *33*, 4451.
(31) Imai, M.; Mori, K.; Mizukami, T.; Kaji, K.; Kanaya, T. *Polymer* **1992**, *33*, 4457.
(32) Klug, H. P.; Alexamder, L. E. *X-ray Diffraction Procedures*; John Wiley & Sons: New York, 1954.
(33) Ruland, W. *Colloid Polym. Sci.* **1977**, *255*, 833.
(34) Daubery, R. D.; Bunn, C. W.; Brown, C. J. *Proc. R. Soc. London, Ser. A* **1954**, *226*, 531.
(35) Lin, D.-J.; Chang, C.-L.; Lee, C.-K.; Cheng, L.-P. *Eur. Polym. J.* **2006**, *42*, 356 .
(36) Fornes, T. D.; Paul, D. R. *Polymer* **2003**, *44*, 3945.
(37) Tung, J.; Gupta, R. K.; Simon, G. P.; Edward, G. H.; Bhattacharya, S. N. *Polymer* **2005**, *46*, 10405.
(38) Shen, H.; Jeong, K.-U.; Xiong, H.; Graham, M. J.; Leng, S.; Zheng, J. X.; Huang, H.; Guo, M.; Harris, F. W.; Cheng, S. Z. D. *Soft Matter* **2006**, *2*, 232 .
(39) Jeong, K.-U.; Yang, D.-K.; Graham, M. J.; Tu, Y.; Kuo, S.-W.; Knapp, B. S.; Harris, F. W.; Cheng, S. Z. D. *Adv. Mater.* **2006**, *18*, 3229.
(40) Liberata, G.; Giuliana, G.; Concetta, D.; Mariarosaria, T.; Vittoria, V.; Pasquale, L.; Stefania, P. *Macromol. Chem. Phys.* **2002**, *203*, 1420.
(41) Salem, D. R. *Polymer* **1992**, *33*, 3182.
(42) Salem, D. R. *Polymer* **1992**, *33*, 3189.
(43) Lee, C. H.; Saito, H.; Inoue, T.; Nojima, S. *Macromolecules* **1996**, *29*, 7034.
(44) Lee, C. H.; Saito, H.; Inoue, T. S. *Macromolecules* **1993**, *26*, 6566.
(45) Hashimoto, T.; Kume, T. *J. Phys. Soc. Jpn.* **1992**, *61*, 1839.
(46) Terrill, N. J.; Fairclough, P. A.; Towns-Andrews, E.; Komanschek, B. U.; Young, R. J.; Ryan, A. *Polymer* **1998**, *39*, 2381.
(47) Olmsted, P. D.; Poon, W. C. K.; Mcleish, T. C. B.; Terrill, N. J.; Ryan, A. *Phys. Rev. Lett.* **1998**, *81*, 373.
(48) Ezquarra, T. A.; López-Cabarcos, E.; Hsiao, B. S.; Baltà-Calleja, F. J. *Phys. Rev. E* **1996**, *54*, 989.
(49) Cakmak, M.; Teitge, A.; Zachmann, H. G.; White, J. L. *J. Polym. Sci, Part B: Polym. Phys.* **1993**, *31*, 371.
(50) Bonart, R.; Hosemann, R. *Kolloid Z. Z. Polym.* **1962**, *186*, 16.
(51) Kubo, H.; Okamoto, M.; Kotaka, T. *Polymer* **1998**, *39*, 4827.
(52) Taiko, H.; Chagin, T.; Kawakami, D.; Goddard, W. A., III *Polym. Prep.* **2004**, *45*, 794.

MA702554T